ON THE ROLE OF THE BACKGROUND OVERLYING MAGNETIC FIELD IN SOLAR ERUPTIONS

A. Nindos[1], S. Patsourakos[1], and T. Wiegelmann[2]
[1] Section of Astrogeophysics, Physics Department, University of Ioannina, Ioannina GR-45110, Greece; anindos@cc.uoi.gr
[2] Max-Planck-Institut für Sonnensystemforschung (MPS), Max-Planck-Strasse 2, Katlenburg-Lindau, Germany

ABSTRACT

The primary constraining force that inhibits global solar eruptions is provided by the overlying background magnetic field. Using magnetic field data from both the Helioseismic and Magnetic Imager aboard the *Solar Dynamics Observatory* and the spectropolarimeter of the Solar Optical Telescope aboard *Hinode*, we study the long-term evolution of the background field in active region AR11158 that produced three major coronal mass ejections (CMEs). The CME formation heights were determined using EUV data. We calculated the decay index $-(z/B)(\partial B/\partial z)$ of the magnetic field B (i.e., how fast the field decreases with height, z) related to each event from the time of the active region emergence until well after the CMEs. At the heights of CME formation, the decay indices were 1.1–2.1. Prior to two of the events, there were extended periods (of more than 23 hr) where the related decay indices at heights above the CME formation heights either decreased (up to -15%) or exhibited small changes. The decay index related to the third event increased (up to 118%) at heights above 20 Mm within an interval that started 64 hr prior to the CME. The magnetic free energy and the accumulated helicity into the corona contributed the most to the eruptions by their increase throughout the flux emergence phase (by factors of more than five and more than two orders of magnitude, respectively). Our results indicate that the initiation of eruptions does not depend critically on the temporal evolution of the variation of the background field with height.

Key words: Sun: corona – Sun: coronal mass ejections (CMEs) – Sun: flares – Sun: magnetic topology – Sun: photosphere

1. INTRODUCTION

Coronal mass ejections (CMEs) are preceded by a long phase (of the order of a few days) during which the magnetic field is progressively stressed and magnetic free energy and magnetic helicity build up. In both resistive and ideal models, CMEs may result from a catastrophic loss of mechanical equilibrium of the plasma contained within the helicity/free energy-charged coronal magnetic field (e.g., see the review by Klimchuk 2001). In active regions, the forces that maintain equilibrium are the magnetic pressure and tension. Due to their enhanced magnetic pressure, structures of strong magnetic fields (be them flux ropes or not) tend to expand into regions of weak field. Equilibrium is preserved if the tension provided by the overlying background field is sufficient to hold in place the structure that tends to expand. Confinement fails when the energy trapped in a coronal structure is sufficient to drive an outward expansion against the overlying field.

Several investigations of the stability of flux ropes have been published (Bateman 1978; Chen 1989; Lin et al. 2002; Török & Kliem 2005, 2007; Kliem & Török 2006; Fan & Gibson 2007; Isenberg & Forbes 2007; Démoulin & Aulanier 2010; Olmedo & Zhang 2010). Usually, in these studies the overlying background magnetic field is quantified by a decay index n

$$n = -\frac{z}{B}\frac{\partial B}{\partial z}, \qquad (1)$$

where B is the field strength and z is the height above the solar surface. The decay index shows how fast the field decreases with height. It has been shown that there exists a critical value n_c where, if $n > n_c$, the flux rope will erupt (Kliem & Török 2006; Fan & Gibson 2007; Török & Kliem 2007; Démoulin & Aulanier 2010; Olmedo & Zhang 2010). The exact threshold lies in the range $1.1 \lesssim n_c \lesssim 2$ (Bateman 1978; Kliem & Török 2006;

Démoulin & Aulanier 2010). Using photospheric potential-field and nonlinear force-free field (NLFFF) extrapolations, Liu (2008) and Cheng et al. (2011), respectively, calculated snapshot values of the decay index of the background field for several eruptive and confined flares. They found that the decay index is larger for eruptive flares than for confined ones.

The question we address in this Letter is whether the long-term evolution of the decay index of the background magnetic field of an active region facilitates the initiation of CMEs. In Section 2, we present our observations and the procedures for their analysis. Section 3 discusses the results from the decay index computations and Section 4 those from the magnetic free energy and helicity computations. A summary and our conclusions are presented in Section 5.

2. OBSERVATIONS AND DATA REDUCTION

Our target was active region AR11158. Its photospheric magnetic field was studied using both line of sight (LOS) and vector magnetograms. The former were full-disk images obtained with the Helioseismic and Magnetic Imager (HMI) aboard the *Solar Dynamics Observatory* (*SDO*) while the latter were obtained with the spectropolarimeter (SP) of the Solar Optical Telescope aboard *Hinode*. The HMI data covered the interval from 2011 February 11 00:00 to February 15 23:59 on a 45 s cadence. During this interval, the SP obtained 16 vector magnetograms of AR11158 on a varying cadence. Unfortunately, there were a few observations where the easternmost and westernmost parts of the active region fell out of the SP field of view.

For the study of the background field, we first have to extrapolate the three-dimensional coronal magnetic field using the observed photospheric magnetograms as the bottom boundaries. We computed potential-field extrapolations using the LOS HMI magnetograms as boundary conditions. For these extrapolations, each magnetogram was obtained 15 minutes apart from
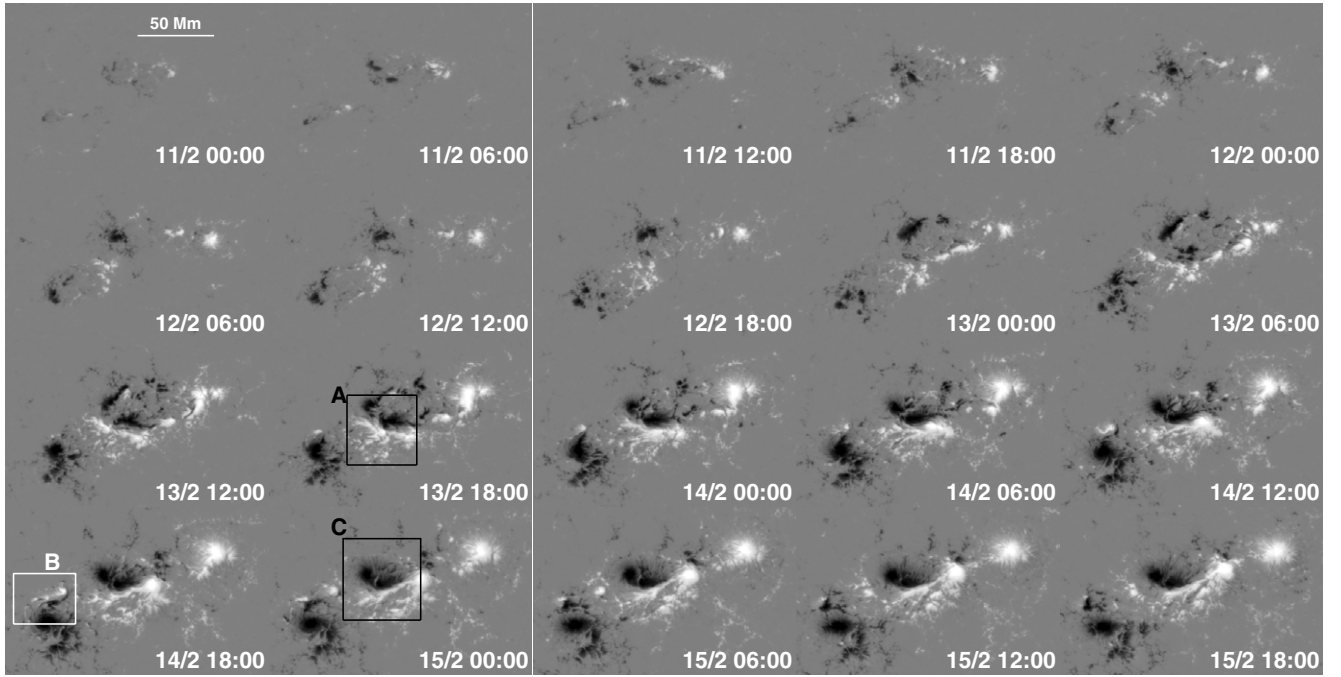
Figure 1. Selected HMI LOS photospheric magnetograms of AR11158 from 2011 February 11 to 15. The regions labeled A, B, and C mark the photospheric bases of the boxes used for the decay index computations at the times of the February 13–15 events, respectively.

the other. The field of view of the bottom boundary was centered around the center of AR11158 and the size of the computation box was $290 \times 205 \times 160$ Mm^3.

We also computed NLFFF extrapolations, using the available SP vector magnetograms as bottom boundaries. The magnetograms were rebinned 2×2 to $0\farcs6$ pixel^{-1}. The dimensions of the computation box were $252 \times 252 \times 252$ pixel^3 which correspond to $110 \times 110 \times 110$ Mm^3. The potential-field data with which the extrapolation code would initialize the computation domain were computed using the method described by De Rosa et al. (2009). In order to reduce the effect of the Lorentz force acting in the photosphere and obtain data that were as close as possible to the measured data, the vector magnetograms were preprocessed using the method developed by Wiegelmann et al. (2006). This procedure minimizes the functional $L_{\mathrm{prep}} = \mu_1 L_1 + \mu_2 L_2 + \mu_3 L_3 + \mu_4 L_4$. The L_1 and L_2 terms contain force-free and torque-free consistency integrals, respectively. The L_3 term ensures that the optimized boundary condition agrees with the measured photospheric data and the L_4 term controls the smoothing. We used $\mu_1 = \mu_2 = 1$, $\mu_3 = 0.001$, and $\mu_4 = 0.01$ which are the optimal values for SP data. The NLFF fields were computed with the "optimization method" (Wheatland et al. 2000) as implemented by Wiegelmann (2004).

3. THE DECAY INDEX OF THE OVERLYING FIELD

The evolution of the photospheric LOS field is presented in Figure 1 (see also Schrijver et al. 2011). Two bipoles emerged in close proximity almost simultaneously on February 11. The flux emergence lasted for almost 90 hr, and then the total flux did not change much. The highest rate of emergence started after February 12 12:00. Converging and shearing motions between the trailing polarity of the northern bipole and the leading polarity of the southern bipole formed a complex bipolar δ spot group close to the middle of the field of view. East and west of it, other spots formed from the development of the southern

and northern bipoles, respectively. These outer spots constituted large-scale bipoles that surrounded the central δ spot group.

During the observations, AR11158 was the site of three major CMEs associated with one X-class and two M-class flares (see Table 1). In addition to these CMEs, several surges occurred from the eastern part of the active region. The formation heights of the CMEs were determined using images from the Extreme Ultraviolet Imager (EUVI) on the *Solar Terrestrial Relations Observatory* spacecraft *Behind* (*STEREO-B*). In these images the active region appeared close to the limb (*STEREO-Ahead* was $86°$ ahead of the Sun–Earth line and *STEREO-B* $94°$ behind). In both the February 13 and 15 events, the EUVI data showed the formation of a bubble-like feature which was the signature of the CME in its infancy. The simulations by B. Kliem et al. (2012, in preparation) imply that the initial size of such EUV bubbles sets an upper limit to the size of the early flux rope. We estimated the height–time profile of each bubble by fitting a circle to its bright outer edge. The heights in Table 1 correspond to the height of the center of each best-fit circle, h_0, and the height of the best-fit front (i.e., the sum of h_0 and the radius of the best-fit circle) when the bubble first appeared. The low coronal signatures of the February 14 event showed flaring loops associated with the peak of the M-class flare and a narrow surge-like feature that was moving away from the surface at an angle of about $20°$ with respect to the apparent east–west direction and later evolved into a CME. The formation heights for this event in Table 1 correspond to the height of the flaring loops and the leading edge of the surge.

At each height, the decay index was calculated from the average of the horizontal component of the field (the vertical component does not contribute to the downward constraining force; Liu 2008) over the corresponding pixels of the computation box related to a given event. The computation boxes were determined as follows. Their heights were equal to the heights of the extrapolation boxes and their bases were in the photosphere and were defined by the regions A, B, and C of Figure 1. The centers of regions A and C were the centers of the EUV
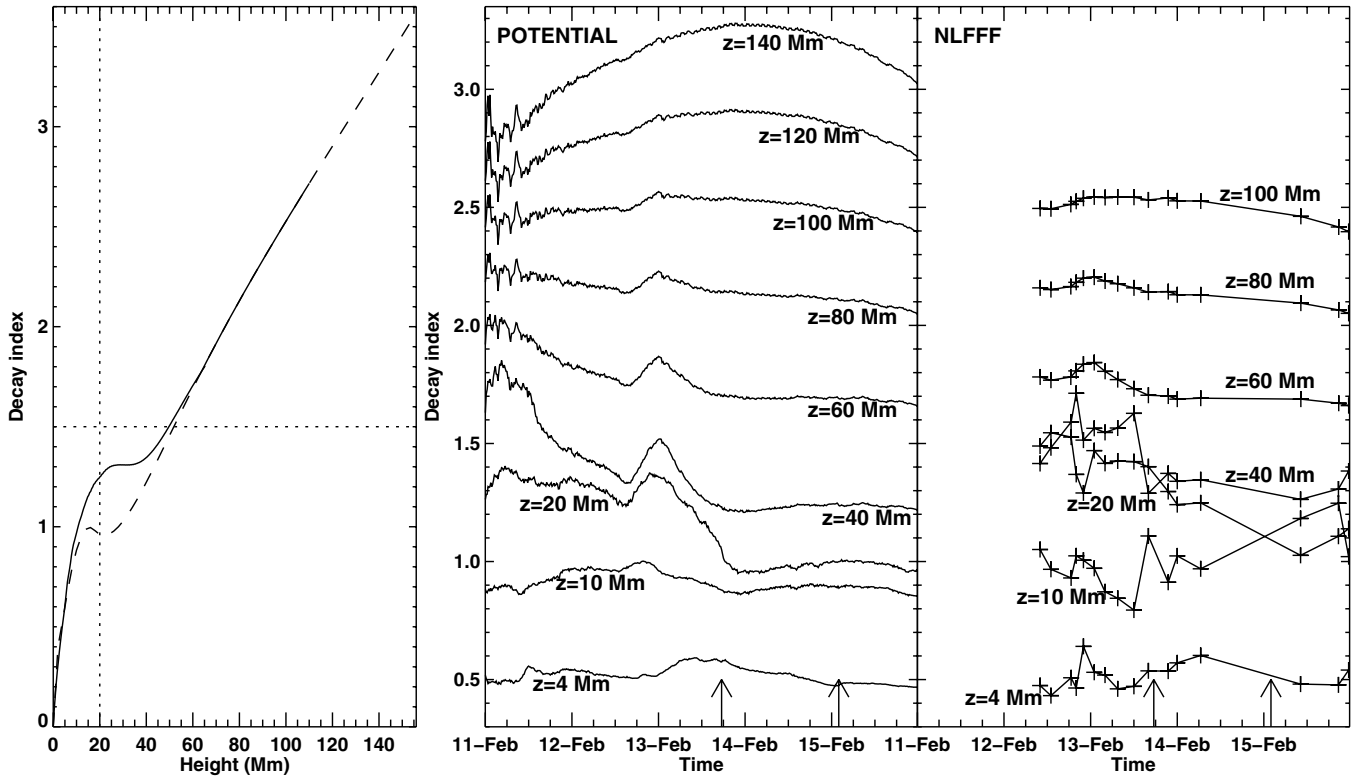
Figure 2. Decay index above region C as it rotated across the disk. Left panel: the decay index as a function of height computed for February 14, 06:30 (time of the last available vector magnetogram before the February 15 event). The solid and dashed lines indicate the results from the NLFFF and the potential-field extrapolations, respectively. The vertical and horizontal dotted lines indicate a height of 20 Mm and a decay index of 1.5, respectively. Middle panel: temporal evolution of the decay index at selected heights resulted from the potential-field extrapolations. The arrows indicate the times of the February 13 and 15 flare maxima. Right panel: same as the middle panel for the decay index from the NLFFF extrapolations.

Table 1
M- and X-class Flares and Major CMEs from AR11158

Event	Flare Peak (UT)	Flare Location	*GOES* Class	CME Formation Height (Mm)	Δn [a] (%)	ΔE_{free} [b] (%)	$\Delta(\Delta H)$ [c] (%)
2011 Feb 13	17:38	S20E04	M6.6	25–50	[−15, 4]	567	5500
2011 Feb 14	17:26	S20W04	M2.2	20–190	[−9, 69]	>767	18600
2011 Feb 15	01:56	S20W12	X2.2	55–80	[−4, 2]	>767	24000

Notes.
[a] Percentage difference between the decay index at CME onset and on February 12 12:00 at heights above CME formation.
[b] Percentage difference between the free energy at CME onset and on February 12 12:00.
[c] Same as (b) for the accumulated helicity.

dimmings related to the February 13 and 15 CMEs, respectively (the borders of the dimmings were defined by visual inspection of 171 Å images taken by the Atmospheric Imaging Assembly aboard *SDO*). The sides of regions A and C were equal to the first measurements of the diameters of the February 13 and 15 bubbles, respectively. No bubble was observed in the February 14 event, and the center of region C was the center of the flare brightening. To account for the oblique propagation of the erupted material, the size of region C was twice the size of the rectangle that contained the flare brightening. Our results were not affected by the oblique propagation because if we doubled the size of C, we would obtain results similar to those presented in this Letter. In order to study the temporal evolution of the decay indices for each event, regions A, B, and C were followed throughout the observations as they rotated across the solar disk.

For the February 13 and 15 events, the decay index was computed using the field resulted from both the potential-field and NLFFF extrapolations. For the February 14 event, only

the potential-field extrapolations were used, because part of the photospheric base of the decay index computation box fell out of the field of view of the vector magnetograms.

In theoretical studies, the background field is separate from the flux rope field (Török & Kliem 2007; Olmedo & Zhang 2010). Such distinction was not done in our study, because (1) in the extrapolated fields, it is difficult to separate the background field from that of the structure that erupts, and (2) we are primarily interested in the long-term evolution of the background field.

The results from the decay index computations are given in Table 1 and for the February 15 and 14 events (i.e., from the computation boxes with bases defined by the regions C and B, respectively, as they rotated across the disk), the results are presented in Figures 2 and 3, respectively. We do not show a figure with the results for the February 13 event because the curves were very similar to those for the February 15 event; we will use Figure 2 for the discussion of the temporal evolution
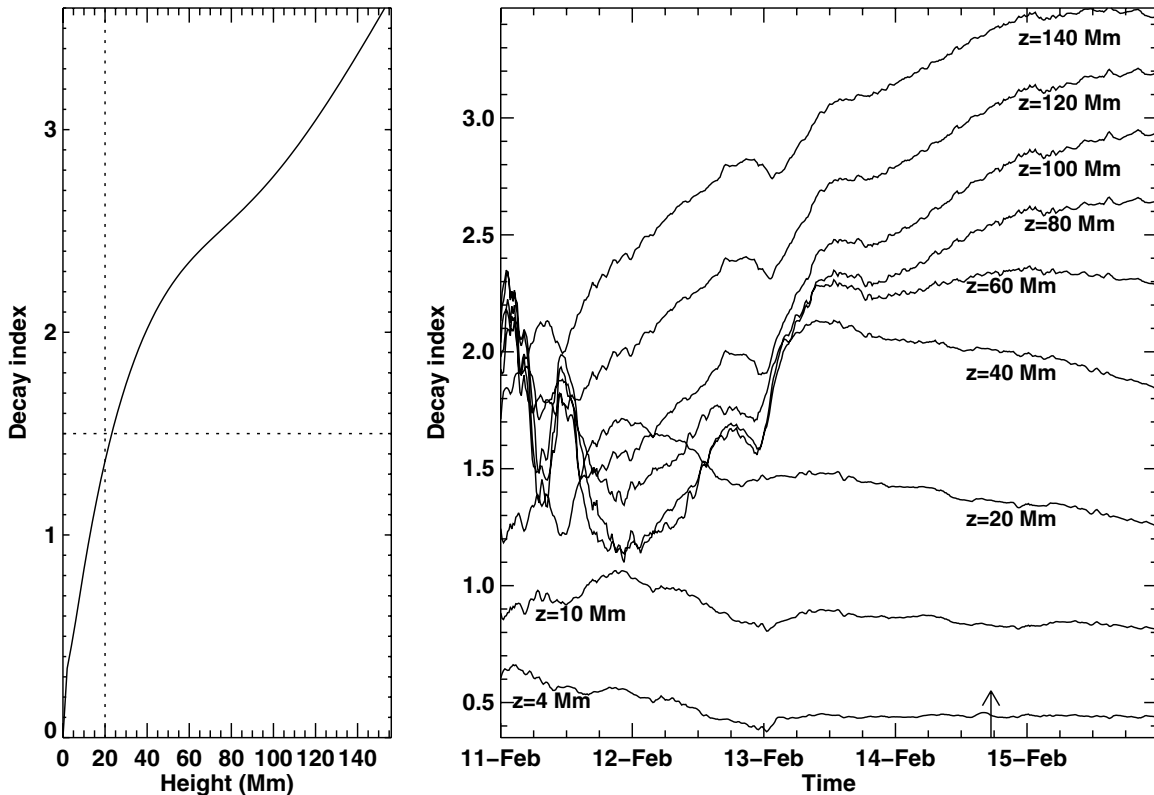
3

Figure 3. Decay index above region B as it rotated across the disk. The format of the figure is the same as that of Figure 2 with the exceptions that the left panel shows the decay index computed for February 14, 17:15, and that no decay index from NLFFF extrapolations is presented. The arrow shows the time of the February 14 flare maximum.

of the decay indices from both A and C. In the left panels of Figures 2 and 3 we show two characteristic examples of the decay indices as a function of height. The other panels show the temporal evolution of the decay indices. A comparison of Figures 2 and 3 indicates that, at a given height greater than about 10 Mm, the decay index associated with the February 14 event is larger than that of the February 15 event.

The left panel of Figure 2 indicates that the decay indices computed from the potential-field and NLFFF extrapolations showed similar variations with height. However, at heights up to about 55–60 Mm, the n from the NLFFF extrapolations showed larger values, due to the higher values of the horizontal component of the field. This is particularly evident around the local maximum of the NLFFF decay index at about 25 Mm. The long-term temporal evolution of the potential-field decay index was consistent with that of the NLFFF decay index. The similarity of the time profiles of the two sets of decay indices became better at heights above 50–60 Mm which may indicate that the field was essentially potential above these heights.

The February 13 CME formed at heights 25–50 Mm where the decay index was in the range 1.1–1.6. Figure 2 shows that at heights of 20–80 Mm, the decay index decreased with time from the beginning of the observations until about February 12 14:30. Then, these time profiles showed a local bump that lasted about 23–27 hr. The bump reflected a decrease and a subsequent increase of the extrapolated horizontal field component. The February 13 CME occurred toward the end of the descending part of the bump. At heights of 25–80 Mm, the decay index at CME onset was smaller than the decay index just before the bump appearance (up to −15% at $z = 25$ Mm). Higher up, the decay index showed a slow increase that lasted for almost 72 hr (from the beginning of the observations until about February

14 00:00). However, at these heights the February 13 bubble was already moving away from the surface with a speed of ∼450 km s^{-1}.

The February 15 CME formed at heights where the decay index was in the range 1.7–2.1. From these heights up to 100 Mm (see Figure 2), there was an extended time interval of more than 32 hr prior to the CME where the temporal changes of the decay index were small. This interval started just after the local bump in the n time profiles and was prolonged until the end of the observations. At heights larger than 100 Mm there was a slow decrease of the decay index from about February 14 00:00 until the end of the observations.

In the February 14 eruption, the nominal critical decay index of torus instability ($n = 1.5$; Török & Kliem 2005) is reached at 25 Mm, which is close to the height of the flaring loops observed in the EUVI data. The time profiles of the decay index showed that at heights larger than 20 Mm, the decay index increased significantly after about February 12 01:00 (up to 118% at 80 Mm). At heights up to 60 Mm, the n increased for about 40 hr and then its changes were small. Higher up, it continued to increase until the end of the observations. The derived increase of the decay index might have facilitated the several surges from the eastern part of the active region that occurred from February 13 onward.

4. THE EVOLUTION OF MAGNETIC HELICITY AND FREE ENERGY

The extended intervals prior to the February 13 and 15 eruptions where the decay index did not increase significantly raise the question of which properties of the magnetic field contributed the most to the eruptions. To this end, we investigated
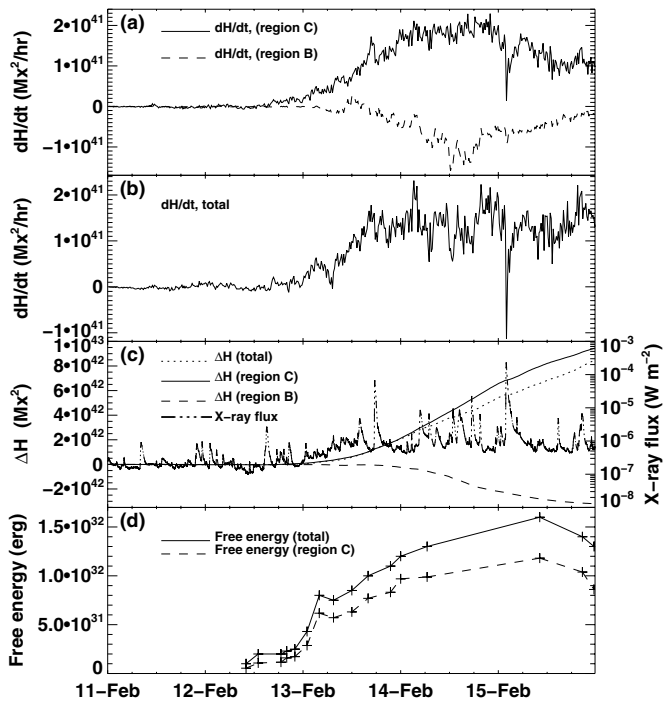
Figure 4. (a) Time profiles of the flux of the injected helicity into regions B and C. (b) Time profile of the net flux of the injected helicity over the entire active region. (c) Time profiles of the net accumulated changes of helicity for the entire active region, and for regions B and C. The *GOES* soft X-ray flux time profile is also presented. (d) Temporal evolution of the magnetic free energy for the entire active region and for region C.

the long-term evolution of both magnetic helicity and free energy in AR11158.

The helicity injected into AR11158 was computed from the HMI magnetograms that were used for the decay index computation. We followed the method described by Pariat et al. (2006) with the exception that the velocities were derived using the DAVE method (Schuck 2006). From the helicity fluxes, dH/dt, we calculated the accumulated change of helicity $\Delta H(t)$ as a function of time. The magnetic free energy, E_{free}, was estimated from the NLFFF and the potential-field extrapolations derived from the SP magnetograms.

Figure 4 indicates that the bulk of the free energy and helicity of AR11158 were associated with its sheared core. There was significant helicity and free energy buildup from about February 12 12:00 until the end of the flux emergence phase (see also Table 1). The local bumps in the time profiles of the decay index prior to the February 13 event (from about February 12 14:30 until about February 13 17:30) partly overlapped the interval from February 13 00:00 until February 14 06:00 of the fastest increase of both the free energy and helicity flux injected into region A (the curve for region A is not shown because it is very similar to that of region C). During the interval of decay index increase prior to the February 14 CME (i.e., from February 12 01:00 until February 14 17:30), the helicity flux injected into region B originally did not change much, but later (after February 13 12:00) attained its fastest increase rate and reached maximum values around the time of the CME. The interval of small decay index temporal changes from February 13 18:00 until the February 15 event corresponded to the largest values of helicity flux injected into region C. At the time of the X-class flare, there was an impulsive decrease of the helicity injection rate. Such impulsive dH/dt components have been observed

in several large flares, but their origin is not clear (Démoulin 2007). The free energy increased until February 15 10:15, but the last available vector magnetogram before the X-class flare was taken on February 14 06:30. Consequently, we cannot tell whether there was any decrease of free energy just after the February 14 and 15 flares.

5. SUMMARY AND CONCLUSIONS

Our study is the first to address the question of whether the long-term evolution of the background field facilitates eruptions. Our target, AR11158, was the site of three major CMEs. EUV observations helped us constrain the formation heights of the CMEs. For each event, the decay index of the field was computed above the photospheric region related to the CME formation. The decay index was determined from potential-field extrapolations every 15 minutes by following these regions as they rotated across the disk for 5 days since the first signs of active region emergence. Similar results were obtained from the NLFFF extrapolations of 16 vector magnetograms.

Our study indicates the following.

1. At the heights of CME formation the decay indices were in the range of 1.1–2.1.
2. The February 13 CME occurred after the descending part of a 23–27 hr long bump in the time profiles of the related decay index at a range of heights from the CME formation heights up to about 1.5 times those heights.
3. The February 15 CME was preceded by a 32 hr long interval where the related decay index at heights equal to or larger than the CME formation heights exhibited small changes ($\lesssim \pm 4\%$).
4. The decay index related to the February 14 event increased up to 118% at heights above 20 Mm within an interval that started 64 hr prior to the CME.
5. Both the magnetic free energy and the accumulated helicity increased throughout the flux emergence phase (by factors of more than five and more than two orders of magnitude, respectively).

The key conclusion of the above results is that the onset of eruptions does not depend critically on the long-term evolution of the decay index of the background field prior to the CMEs. Our results do not necessarily imply that the overlying field is not removed (removal can happen, e.g., by reconnection between the emerging and the overlying field). They merely suggest that the initiation of eruptions does not depend critically on the temporal evolution of the variation of the ambient field with height. Our results are consistent with the numerical experiments by Archontis & Török (2008), who simulated the eruption of a coronal flux rope when emerging magnetic field reconnects with a horizontal ambient field that does not vary with height.

REFERENCES

Archontis, V., & Török, T. 2008, A&A, 492, L35
Bateman, G. 1978, MHD Instabilities (Cambridge, MA: Massachusetts Institute of Technology)
Chen, J. 1989, ApJ, 338, 453
Cheng, X., Zhang, J., Ding, M. D., Guo, Y., & Su, J. T. 2011, ApJ, 732, 87
Démoulin, P. 2007, Adv. Space Res., 39, 1674
Démoulin, P., & Aulanier, G. 2010, ApJ, 718, 1388

De Rosa, M. L., Schrijver, C. J., Barnes, G., et al. 2009, ApJ, 696, 1780
Fan, Y., & Gibson, S. E. 2007, ApJ, 668, 1232
Isenberg, P. A., & Forbes, T. G. 2007, ApJ, 670, 1453
Kliem, B., & Török, T. 2006, Phys. Rev. Lett., 96, 255002
Klimchuk, J. A. 2001, in Space Weather, ed. P. Song, H. J. Singer, & G. L. Siscoe (Geophysics Monograph 125; Washington, DC: AGU), 143
Lin, J., van Ballegooijen, A. A., & Forbes, T. G. 2002, J. Geophys. Res., 107, 1438
Liu, Y. 2008, ApJ, 679, L151
Olmedo, O., & Zhang, J. 2010, ApJ, 718, 433

Pariat, E., Nindos, A., Démoulin, P., & Berger, M. A. 2006, A&A, 452, 623
Schrijver, C. J., Aulanier, G., Title, A. M., Pariat, E., & Delannée, C. 2011, ApJ, 738, 167
Schuck, P. W. 2006, ApJ, 646, 1358
Török, T., & Kliem, B. 2005, ApJ, 630, L97
Török, T., & Kliem, B. 2007, Astron. Nachr., 328, 743
Wheatland, M. S., Sturrock, P. A., & Roumeliotis, G. 2000, ApJ, 540, 1150
Wiegelmann, T. 2004, Sol. Phys., 219, 87
Wiegelmann, T., Inhester, B., & Sakurai, T. 2006, Sol. Phys., 233, 215